

On the interplay of photons and charge carriers in thin-film solar cells

Pyry Kivisaari, Mikko Partanen, Toufik Sadi, and Jani Oksanen
Engineered Nanosystems Group, Aalto University, P.O. Box 13500, FI-00076 Aalto, Finland

Thin films are gaining ground in photonics and optoelectronics, promising improvements in their efficiency and functionality as well as decreased material usage as compared to bulk technologies. However, proliferation of thin films would benefit not only from continuous improvements in their fabrication, but also from a unified and accurate theoretical framework of the interplay of photons and charge carriers. In particular, such a framework would need to account quantitatively and self-consistently for photon recycling and interference effects. To this end, here we combine the drift-diffusion formalism of charge carrier dynamics and the fluctuational electrodynamics of photon transport self-consistently using the recently introduced interference-extended radiative transfer equations. The resulting equation system can be solved numerically using standard simulation tools, and as an example, here we apply it to study well-known GaAs thin-film solar cells. In addition to obtaining the expected device characteristics, we analyze the underlying complex photon transport and recombination-generation processes that represent a full solution to the inhomogeneous Maxwell's equations and that are generated directly as a result of solving the self-consistent model. The methodology proposed in this work is general and can be used to obtain accurate physical insight into a wide range of planar optoelectronic devices, of which the thin-film single-junction solar cells studied here are only one example.

Keywords: Thin-film solar cells, Photon recycling, Fluctuational electrodynamics

I. INTRODUCTION

Photonics and optoelectronics have irrevocably transformed several areas of society, including energy production through solar cells, general lighting through light-emitting diodes, and high-speed Internet through global optical fibre networks.¹⁻³ As these technologies mature and become established, new structures and device concepts are emerging both to increase the efficiency of existing technologies and to create new application areas. One such emerging technology is thin and ultra-thin solar cells incorporating 0.1-10 μm thick semiconductor films that enable, e.g., reusing the growth substrate several times and taking advantage of optical cavity effects.⁴⁻⁹ However, taking full advantage of these possibilities still requires improved theoretical understanding, in particular in self-consistently accounting for the interplay between the photons and the charge carriers as well as in combining wave optical resonance effects with the quantum optical loss mechanisms. Without quantitative description of these effects it is not possible to fully access e.g. the intricate photon recycling effects present in high efficiency devices. Developing such models for a tractable simulation framework is therefore one of the major challenges for the further development of the field.¹⁰ To that end, in this paper we propose an accurate, fully self-consistent and generally applicable electro-optical modeling tool for planar thin-film optoelectronic devices, including photon recycling and all interference effects.

Due to its general importance, electro-optical simulation of resonant optoelectronic devices has been a topic of research already for some decades, and recent years have witnessed increased activity thanks to advances in thin-film device fabrication. The wide range the topic makes it unfeasible to give a complete literature review

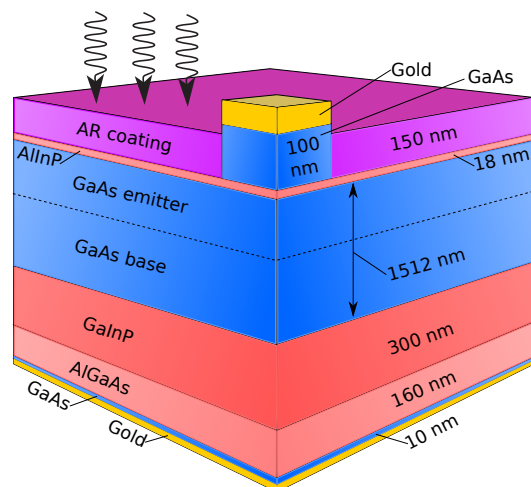


FIG. 1: Thin-film solar cell structure studied in this paper using the proposed interference radiative transfer–drift-diffusion (IRTDD) model.

of it in a research article, but to give an idea of the state of the art, here we refer to two recent works with very similar objectives and device structures as in this work. In Ref. 11, Wilkins *et al.* used transfer matrices to calculate coupling matrices to account for photon recycling and luminescent coupling in drift-diffusion (DD) simulations, and in Ref. 12 Walker *et al.* calculated position-dependent dipole emission in a layer structure to scale the local radiative recombination coefficient and to create a photon redistribution matrix to be used in the DD simulation. Summarizing from these, one typically starts with optical solution methods, such as transfer or scattering matrices or finite-difference time-domain simulations, to create coupling matrices or other constructions relating

emission and absorption locations with each other. These are then used in the carrier dynamics simulation to account for electro-optical effects such as photon recycling. However, previous works have not allowed straightforward modeling of all the spectral, directional and resonant effects in the generation-recombination profiles of the structures. The aim of this paper is to achieve this by creating a direct modeling tool where the optical and electrical properties are solved simultaneously, either using a direct or iterative solver.

The full electro-optical device modeling tool proposed in this paper is implemented by combining the well-known DD model with fluctuational electrodynamics using the recently introduced interference-extended radiative transfer (IRT) model.¹³ Unlike the conventional radiative transfer equation,¹⁴ the IRT model includes all wave-optical and photon recycling effects self-consistently as determined by both the external optical field boundary conditions and the applied bias. The main benefit of the model is that instead of having to use intermediate coupling structures and possible simplifications, here we have a set of differential equations whose self-consistent solution directly satisfies both Maxwell's equations and DD equations. To demonstrate the model with a well-known device structure, here we apply it to simulate the thin-film solar cell structure studied in Ref. 15. By doing this, we wish to illustrate the insight that can be gained with the proposed interference radiative transfer-drift-diffusion (IRTDD) model, and how it can be used to gain detailed physical understanding of essentially any planar optoelectronic device.

II. THEORY

In this Section, we describe the IRTDD model used to carry out fully self-consistent electro-optical simulations of thin-film optoelectronic devices. Present version of the model combines the quantized fluctuational electrodynamics (QFED) framework directly with charge-carrier dynamics as governed by the DD equations, but we expect that a similar IRTDD model could also be derived from the classical fluctuational electrodynamics. We start by writing the IRT model in a somewhat simplified form for a given polarization as¹³

$$\begin{cases} \frac{d}{dz}\phi(z, K, \omega) &= -\alpha(z, K, \omega)[\phi(z, K, \omega) - \eta(z, \omega)] \\ &+ \beta(z, K, \omega)[\phi(z, K, -\omega) - \eta(z, \omega)] \\ S(z, K, \omega) &= \frac{1}{2}\hbar\omega v(z, K, \omega)\rho(z, K, \omega) \\ &\times [\phi(z, K, \omega) - \phi(z, K, -\omega)]. \end{cases} \quad (1)$$

The first part of Eq. (1) is the interference-extended radiative transfer equation for the photon number ϕ of a mode described by its in-plane wave number K and angular frequency ω (with $-\omega$ here denoting the modes propagating towards the negative direction, i.e. downwards in Fig. 1), z is position coordinate in the normal direc-

tion, α and β are the damping and scattering coefficients formulated with help of the dyadic Green's functions as in,¹³ and $\eta(z, \omega)$ is the Bose-Einstein distribution function $\eta = 1/(e^{(\hbar\omega - e\Delta E_F)/(k_B T)} - 1)$ that acts as a local radiative source term.¹⁶ Here e is the elementary charge and ΔE_F is the local quasi-Fermi level separation.

The second part of Eq. (1) relates the photon number with the spectral radiance S in the direction determined by K and ω . Here ρ is the local density of states as defined in,^{13,17} and v is the generalized speed of light defined in Appendix A. As the quantities v , ρ , α and β are derived from fluctuational electrodynamics, they capture all wave-optical effects such as internal reflections, constructive and destructive interferences and emission enhancement and suppression, and they are geometry dependent. The local generation-recombination rate can be calculated with help of the derivative of $S(z, K, \omega)$ as

$$R_r = \sum_{pol.} \int_0^\infty d\omega \int_0^\infty dK \frac{dS}{dz} \frac{1}{\hbar\omega} 2\pi K, \quad (2)$$

where the sum is taken over the two orthogonal polarizations of light. The derivative of S is trivial to calculate using the chain rule and the equations provided in.¹³ Furthermore, we have recently introduced a straightforward way to calculate the dyadic Green's function, the local and nonlocal optical densities of states, and the α and β coefficients for arbitrary planar structures with help of optical admittances,¹⁸ and it is used also in this paper.

The IRT can be readily coupled with the DD model of carrier transport, given by

$$\begin{aligned} \frac{d}{dz}(-\varepsilon \frac{d}{dz}U) &= e(p - n + N_d - N_a) \\ \frac{d}{dz}J_n &= \frac{d}{dz}(\mu_n n \frac{d}{dz}E_{Fn}) = e(R_r + R_{nr}) \\ \frac{d}{dz}J_p &= \frac{d}{dz}(\mu_p p \frac{d}{dz}E_{Fp}) = -e(R_r + R_{nr}), \end{aligned} \quad (3)$$

where ε is the static permittivity, U is the electrostatic potential, e is the elementary charge, n, p are the electron and hole densities, N_d, N_a are the ionized donor and acceptor densities, J_n, J_p are the electron and hole current densities, μ_n, μ_p are the electron and hole mobilities E_{Fn}, E_{Fp} are the conduction and valence band quasi-Fermi levels such that $\Delta E_F = E_{Fn} - E_{Fp}$, and R_{nr} is the nonradiative recombination rate calculated as a sum of Shockley-Read-Hall and Auger recombination as in.¹⁹ Radiative recombination-generation R_r is calculated from the photon numbers using Eq. (2), and therefore the resulting IRTDD model constructed by Eqs. (1) and (3) solves photon and charge carrier dynamics self-consistently.

The boundary conditions and integration limits required for the IRTDD model can be chosen as follows. For each photon energy, the IRT simulation is run for an equally-spaced set of K between zero and suitably chosen $K > Nk_0$, where N is the largest refractive index present in the semiconductor layers. According to the results of this paper, spectral radiances and generation-recombination rates all go to zero at $K > Nk_0$ as expected, indicating that the simulations span all relevant

optical modes. For the DD model, the boundary conditions for the electrostatic potential and quasi-Fermi levels are determined by the built-in potential and applied bias in the conventional way. In particular, the quasi-Fermi levels of electrons and holes are equal with each other at the contacts, corresponding to infinitely fast contact recombination of minority carriers that reach the opposite contact. For incoming solar light, we use the light intensity according to the typical ASTM G173 global reference spectrum²⁰ to enable direct comparison with device characteristics reported elsewhere. In this work, the incoming solar intensity is fully projected into the normally incident modes for simplicity.

III. RESULTS & DISCUSSION

To demonstrate the IRTDD model with a widely known and well-studied example device structure, we simulate a thin-film GaAs solar cell structure similar to the one studied in Ref. 15 and shown schematically in Fig. 1. The device operation is simulated both under dark current conditions and under direct sunlight hitting the sample at normal incidence. The material parameters and the dielectric functions used in the simulations are specified in Appendix B. We start by presenting the overall device characteristics resulting from the IRTDD simulation and proceed to studying the internal photon transport and generation-recombination properties under illumination and in dark current conditions. For the present purposes, we limit the geometry to be fully planar and homogeneous in the lateral direction. Most importantly, here this means that similar to Ref. 12, the sparse top contact grid is not included in the optics calculation. It is, however, expected that the results and the model can be generalized for higher dimensional geometries or light scattering surfaces by separately accounting for lateral effects and extending the boundary conditions.

A. Overall device characteristics

Beginning with the overall device operation, Fig. 2 shows the current-voltage characteristics from the full IRTDD simulation both under illumination and under dark current conditions. The photocurrent curve shows the expected high-efficiency GaAs solar cell characteristics with a short-circuit current of 30.47 mA/cm², open-circuit voltage of 1.09 V, fill factor of 0.88 and maximum power efficiency of 0.29. All these values are close to the experimental and theoretical values reported in,¹⁵ with the main differences likely to result from slightly different simulation or material parameters, and possibly also from optical interference and carrier transport effects that were not included in the calculations of.¹⁵ By a closer inspection, the current-voltage characteristics follow roughly the superposition principle $J(V_a) = J_{sc} + J_{dark}(V_a)$, where J is the total current, V_a is the

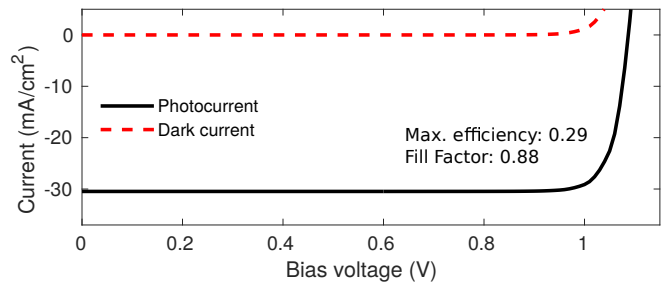


FIG. 2: Current-voltage characteristics of the structure simulated with the IRTDD model in dark and under normally incident sunlight corresponding to the ASTM G173 global reference spectrum.

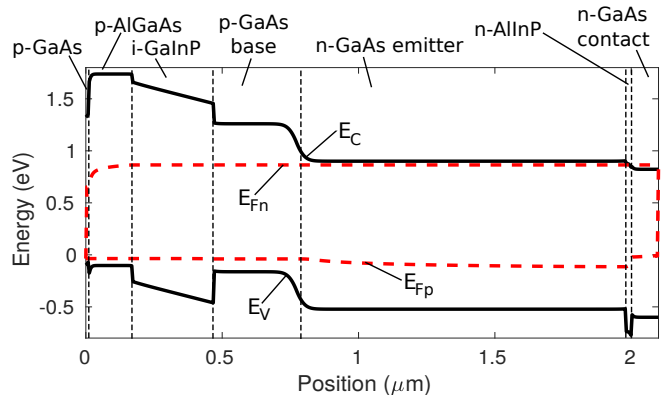


FIG. 3: Band diagram of the structure simulated with the IRTDD model under illumination and an applied bias of 0.9 V.

applied bias, and J_{sc} and J_{dark} are the short-circuit and dark currents.

B. Characteristics under illumination

To study the device operation under illumination, Fig. 3 shows the band diagram of the structure under illumination at an applied bias of 0.9 V. The voltage 0.9 V is chosen for all the following figures to represent an example case where the device still operates fully as a solar cell, and the different layers are marked in the figure for easier interpretation. The band diagram starts at the p-doped GaAs bottom layer and ends at the n-doped GaAs top layer. The left side of the band diagram is clearly p-type with large potential barriers for electrons to prevent them from leaking to the p-contact. The GaAs pn junction formed by the GaAs base and emitter layers is clearly visible in the middle of Fig. 3, and the AlInP layer on the right creates a potential barrier to the valence band to prevent holes from leaking to the n-contact.

For a detailed look at the absorption of sunlight in the structure, Fig. 4 shows a colormap of the generation rate due to solar photons as a function of photon energy and position. At low photon energies below roughly

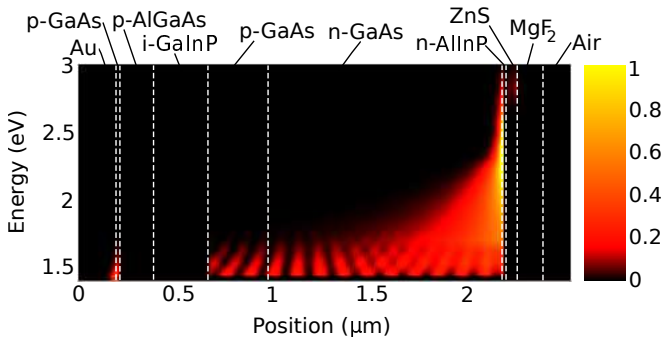


FIG. 4: Generation rate (a.u.) due to incoming solar photons as a function of photon energy and position (with positive values denoting generation). Here, the ZnS and MgF₂ layers constitute the antireflective (AR) coating marked in Fig. 1.

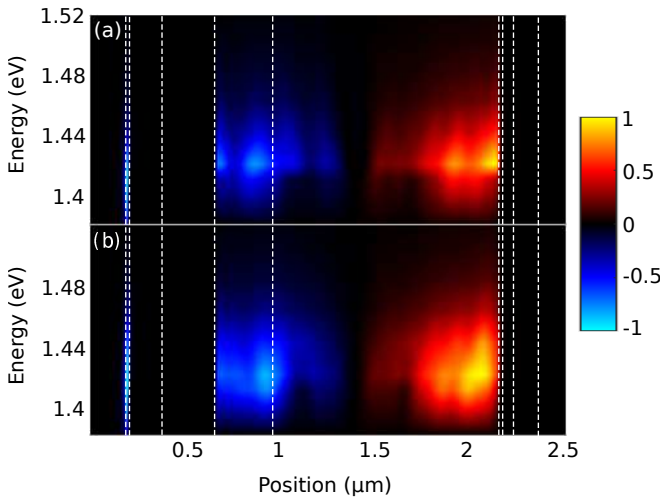


FIG. 5: Total recombination-generation rate (a.u.) due to internal emission as a function of photon energy and position for (a) TE polarization and (b) TM polarization at an applied bias of 0.9 V under illumination (with positive values denoting recombination). For this device configuration and bias, there is a very clear spatial separation between regions of net generation and net recombination. Stronger absorption of sunlight towards the top surface creates an imbalance in carrier densities, which is balanced here by recombination at around 2 μm and a corresponding generation at around 1 μm .

2 eV, generation takes place throughout the GaAs layers due to the modest absorption coefficient and thereby a large contribution also from back-reflected photons. Quite interestingly, there is a clear interference pattern at the lowest photon energies due to the interplay between leftward-propagating photons and the rightward-propagating ones reflected from the gold contact. At photon energies above roughly 2 eV, the generation takes place clearly more towards the top contact on the right side of the figure, as the absorption coefficient of GaAs is large at these photon energies and photons do not reach the lower layers.

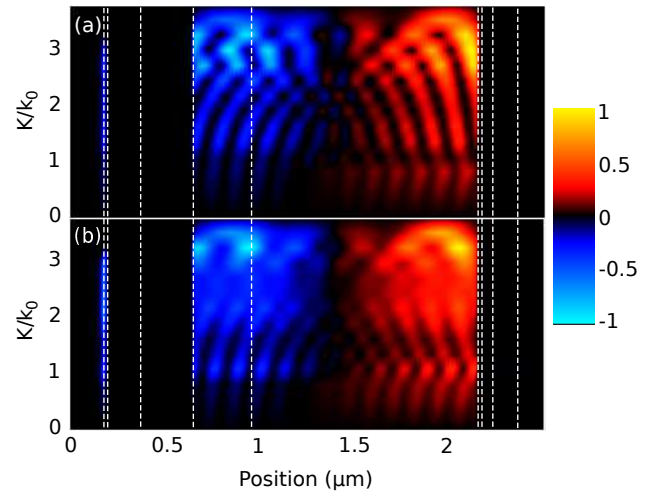


FIG. 6: Recombination-generation rate (a.u.) due to internal emission as a function of K and position at photon energy 1.43 eV at an applied bias of 0.9 V under illumination for (a) TE and (b) TM polarization (with positive values denoting recombination). The rates include the integration factor $2\pi K$.

Turning our attention more towards photon recycling, all the figures from now on describe the net recombination-generation (RG) after subtracting the generation created by the incident light. This will also enable a more direct comparison with the corresponding figures under dark current, which are studied later in Subsection III C. To look at the resulting internal RG characteristics, Fig. 5 shows the RG rate as a function of position and photon energy at an applied bias of 0.9 V under solar illumination. More specifically, Fig. 5(a) shows the RG rate normalized with its maximum value for TE polarization, and Fig. 5(b) shows the same rate for the TM polarization. Comparing TE and TM in Figs. 5(a) and (b), they share the same qualitative characteristics, in which the internal net RG rate is positive (corresponding to net recombination) close to the right side of the figure and negative (corresponding to net generation) towards the left side of the figure. This photon recycling process is caused by the spatially uneven absorption of solar photons in Fig. 4, which causes ΔE_F to be slightly larger next to the top contact than elsewhere in the device. Additionally, the internal recombination-generation in Fig. 5 mostly takes place at photon energies notably below 1.5 eV, as the Fermi-Dirac distributions decay fast as a function of the recombination energy. There are also visible quantitative differences between the TE and TM RG rates in Fig. 5 due to wave-optical effects. For example, the maxima and minima of the RG rate occur at somewhat different locations in (a) and (b) due to the different mode structure of the TE and TM polarizations.

To take a more detailed look at one relevant photon energy, Fig. 6 shows the RG rate as a function of K at 1.43 eV (a value close to the GaAs bandgap energy) for (a) TE and (b) TM polarization. To compare with the previous figure, the row at 1.43 eV in Fig. 5 represents the inte-

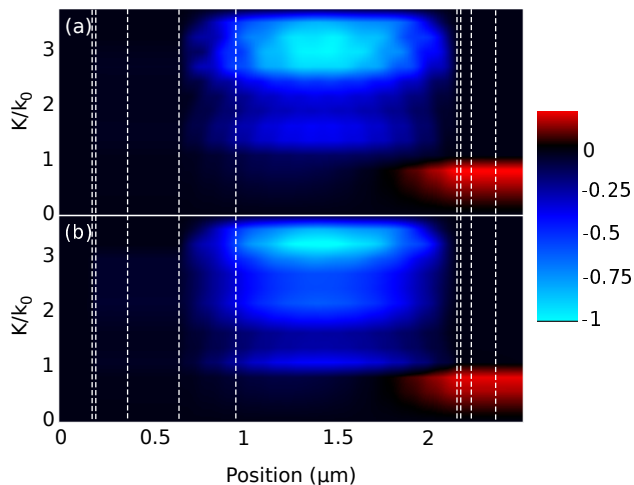


FIG. 7: Spectral radiance $S \times 2\pi K$ (a.u.) as a function of K and position at photon energy 1.43 eV at an applied bias of 0.9 V under illumination for (a) TE and (b) TM polarization.

gral of Fig. 6 over all K . Figure 6 naturally exhibits the same trend in the spatial distribution as Fig. 5, where the RG rate is positive towards the top contact on the right side and negative towards the bottom contact on the left side. Moreover, here the interference effects are clearly visible as spatial oscillations in the RG rate due to constructive and destructive interferences and possibly also due to the Purcell effect. The RG rates approach zero roughly at $K/k_0 = 3.5$, when no more propagating modes exist in the structure. It is noteworthy that the rather complex spatial RG rates shown here are practically impossible to calculate without detailed optical models of emission and photon recycling. As such, they have not previously been reported in this level of detail due to the difficulty to simultaneously account for all the underlying physical processes. In the model proposed here, the RG rates are obtained as a direct result of solving the coupled equation system. We expect this to be beneficial for understanding and optimizing the internal electrical and optical properties of various thin-film devices, such as the emerging ultra-thin GaAs photovoltaic devices,^{21–23} and to complement existing advanced modeling and characterization frameworks of multi-junction solar cells.^{10,24}

To study how the optical power propagates within the solar cell structure studied here, Fig. 7 shows the the K -resolved spectral radiance of internally emitted photons as a function of position and K at the same photon energy 1.43 eV for (a) TE and (b) TM polarization, again for 0.9 V. It can be seen that in the escape cone determined by $K/k_0 \leq 1$, there is a clear positive optical power flow out of the device in the bottom right corner of the figures. However, based on a closer inspection of the results it is only around 0.1 % of the incoming solar optical power, indicating that the structure is still operating fully as a solar cell at this bias. At larger K values, the power escaping the structure becomes zero, but the spec-

tral radiance is negative in the middle of the GaAs layers, corresponding to the RG profiles in the previous figures which show that light is emitted close to the top contact on the right side and absorbed in the lower GaAs layers on the left side due to the imbalance in ΔE_F created by sunlight. This illustrates once more how the internal recombination-generation evens up part of the imbalance in the carrier densities created by solar absorption.

C. Characteristics under dark current

In this Section, we repeat the internal RG results for the dark current case to show that even if the superposition principle holds roughly for the total current, the internal properties of the solar cell under illumination and under dark current conditions can be quite different. The information in Fig. 5 is repeated for dark current conditions in Fig. 8, which again shows the RG rate density as a function of photon energy and position for (a) TE and (b) TM at the bias voltage of 0.9 V. Interestingly, the result is very different from the one shown in Fig. 5 calculated at a similar voltage under solar illumination. In the GaAs region of Fig. 8, we only see positive net RG rates, whereas in Fig. 5 under illumination, there was also a negative RG rate towards the bottom of the GaAs layer on the left, corresponding to net generation there. In the dark current case shown in Fig. 8, there is no clear imbalance in the electron-hole densities created by solar absorption. Therefore net emission is created primarily through the process of radiation out from the structure, and partly through photons that are absorbed by the bottom contact. This difference in the internal optical properties between illuminated and dark operating conditions has been discussed also in Ref. 25.

The RG rate in dark current conditions can be studied in more detail with help of Fig. 9, which repeats the RG rates of Fig. 6 in dark as a function of K and position for (a) TE and (b) TM for a single energy 1.43 eV, again at 0.9 V. It can be seen that there is significant nonzero net recombination only in the modes up to $K/k_0 = 1$, corresponding primarily to photons that radiate out from the structure and partly to photons absorbed by the bottom contact. Above $K/k_0 = 1$, there is only modest recombination resulting in photons that are absorbed by the bottom contact on the left. This observation is further backed up in Fig. 10, which repeats Fig. 7 in dark for (a) TE and (b) TM modes as a function of K and position. Here the spectral radiance has its clearly largest absolute values at $K/k_0 < 1$, corresponding to photons exiting through the AR coating on the right side of the figure and at angles close to escape cone boundaries in particular. However, as seen in the current-voltage characteristics, these internal differences between the dark current case and the case under illumination do not cause the superposition principle to falter visibly, but they certainly introduce effects that might be relevant for some geometries with, e.g., a smaller to-

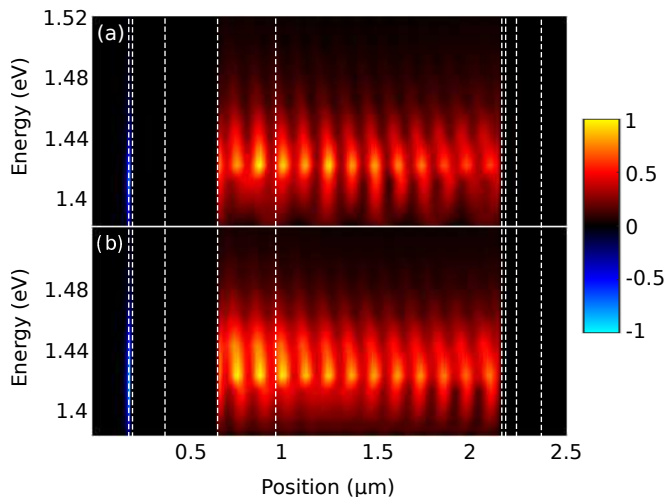


FIG. 8: Information in Fig. 5 repeated for dark current conditions: recombination-generation rate (a.u.) due to internal emission as a function of photon energy and position at an applied bias of 0.9 V under dark current conditions, including all propagation directions: (a) TE and (b) TM polarization.

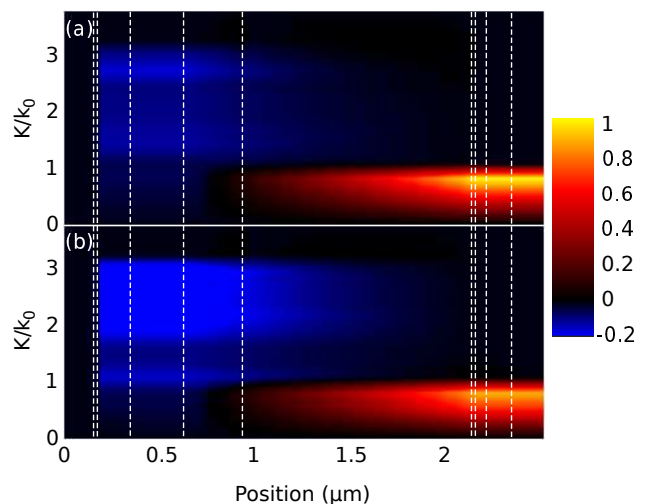


FIG. 10: Information in Fig. 7 repeated for dark current conditions: spectral radiance $S \times 2\pi K$ (a.u.) as a function of K and position at photon energy 1.43 eV at an applied bias of 0.9 V under dark current conditions for (a) TE and (b) TM polarization.

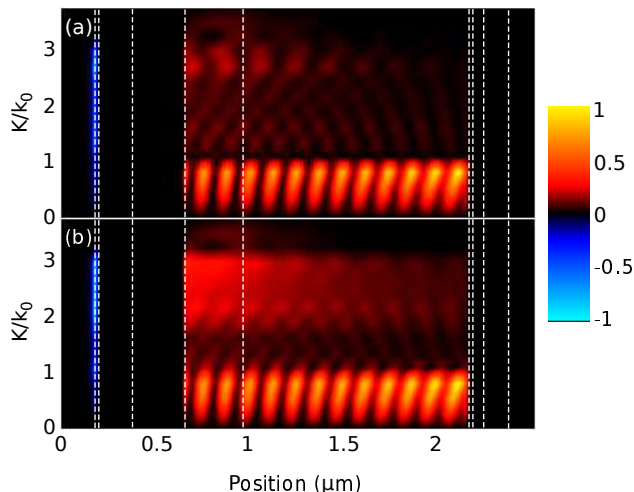


FIG. 9: Information in Fig. 6 repeated for dark current conditions: recombination-generation rate (a.u.) due to internal emission as a function of K and position at photon energy 1.43 eV at an applied bias of 0.9 V under dark current conditions for (a) TE and (b) TM polarization. The rates include the integration factor $2\pi K$.

tal device thickness. In the case under illumination, the re-emission and recycling of absorbed solar photons is not primarily a loss process in the absence of substantial non-radiative recombination, as it merely redistributes part of the solar generation more evenly throughout the whole GaAs active region.

IV. CONCLUSIONS

To improve the theoretical insight into various thin-film optoelectronic devices, we introduced an accurate and fully self-consistent model of photon and charge carrier transport applicable to planar devices. The model was based on connecting the drift-diffusion formalism of carrier transport and fluctuational electrodynamics of photon transport by making use of the newly developed interference-extended radiative transfer equations. To demonstrate the thus obtained IRTDD modeling tool, we applied it to study the device characteristics and internal optical properties of a thin-film GaAs solar cell. The results indicate that the IRTDD model not only reproduces the expected device characteristics, but also directly provides detailed physical insight into complex nonlocal effects such as photon recycling, which is a relevant process particularly in high-efficiency thin-film solar cells. The IRTDD framework presented here is general, and it could be implemented in a wide range of planar resonant devices for detailed studies of photon recycling, luminescent coupling and other complex forms of electro-optical interaction.

Acknowledgments

We acknowledge financial support from the Academy of Finland (grant number 315403) and the European Research Council (Horizon 2020 research and innovation programme, grant agreement No 638173).

Appendix A: Modified photon numbers and related quantities

To use the IRT model in solar cells and other devices, it is convenient if the incoming photon numbers can be set to zero at the outer boundaries of the computational

domain as a boundary condition. To this end, we slightly modify the definition of the interference density of states (IFDOS) as compared to the one used in.¹³ Using the notation of,¹³ we begin by writing the spectral radiance as

$$\langle \hat{S}_\sigma(z, K, \omega) \rangle = \hbar \omega v_\sigma(z, K, \omega) \int_{-\infty}^{\infty} \rho_{IF,\sigma}(z, K, \omega, z') \langle \hat{\eta}(z', \omega) \rangle dz', \quad (\text{A1})$$

where the generalized velocities of light are given by

$$v_{TE} = \frac{2ck_0|\mu|\Re(k_z/\mu)}{|k|^2 + |k_z|^2 + K^2}, \quad v_{TM} = \frac{2ck_0|\varepsilon|\Re(k_z/\varepsilon)}{|k|^2 + |k_z|^2 + K^2}. \quad (\text{A2})$$

These changes in the velocities are balanced by scaling the IFDOSs with a factor $\zeta_{v,\sigma} = c/(v_\sigma n_r)$. The value of the spectral radiance is unchanged, but the IFDOSs and the related propagating photon numbers are slightly modified as specified below. Making use of the photon numbers propagating in the positive or negative direction instead, the spectral radiance is written as in Eq. (1). With this choice of v_σ , we obtain that outside the simulation domain, $\alpha_+ = \text{const.}$ in the negative direction, $\alpha_- = \text{const.}$ in the positive direction, $\beta_+ = 0$ in the negative direction, and $\beta_- = 0$ in the positive direction. In addition, the mentioned constant values of α_+ and α_- are zero in lossless media. This allows one to set the input photon numbers to zero in all lossy and lossless cases when there are no sources outside.

Another difference with¹³ is the definition of the IFDOSs, which are here given by

$$\rho_{IF,TE}(z, K, \omega, z') = -\frac{\omega^3}{2\pi^3 c^3 v_{TE}} \Im [\varepsilon'_i g_{ee}^{11} g_{me}^{21*} + \mu'_i g_{mm}^{22} g_{em}^{12*} + \mu'_i g_{mm}^{23} g_{em}^{13*}], \quad (\text{A3})$$

$$\rho_{IF,TM}(z, K, \omega, z') = \frac{\omega^3}{2\pi^3 c^3 v_{TM}} \Im [\mu'_i g_{mm}^{11} g_{em}^{21*} + \varepsilon'_i g_{ee}^{22} g_{me}^{12*} + \varepsilon'_i g_{ee}^{23} g_{me}^{13*}]. \quad (\text{A4})$$

To derive the IRT coefficients, the derivatives of the IFDOSs are given by

$$\begin{aligned} \frac{\partial \rho_{IF,TE}}{\partial z} = & -\frac{\omega^4}{2\pi^3 c^4 v_{TE}} \left[\Im \left[\frac{\varepsilon k_z^2}{k^2} \right] (\varepsilon'_i |g_{ee}^{11}|^2 + \mu'_i |g_{em}^{12}|^2 + \mu'_i |g_{em}^{13}|^2) + \mu_i (\varepsilon'_i |g_{me}^{21}|^2 + \mu'_i |g_{mm}^{22}|^2 + \mu'_i |g_{mm}^{23}|^2) \right] \\ & + \frac{\omega^2 n_r}{2\pi^3 c^3} \Im \left[\varepsilon_i g_{ee}^{11} + \mu_i g_{mm}^{22} + \mu_i \frac{\mu^2}{|\mu|^2} g_{mm}^{33} \right] \delta(z - z'), \end{aligned} \quad (\text{A5})$$

$$\begin{aligned} \frac{\partial \rho_{IF,TM}}{\partial z} = & -\frac{\omega^4}{2\pi^3 c^4 v_{TM}} \left[\Im \left[\frac{\mu k_z^2}{k^2} \right] (\mu'_i |g_{mm}^{11}|^2 + \varepsilon'_i |g_{me}^{12}|^2 + \varepsilon'_i |g_{me}^{13}|^2) + \varepsilon_i (\mu'_i |g_{em}^{21}|^2 + \varepsilon'_i |g_{ee}^{22}|^2 + \varepsilon'_i |g_{ee}^{23}|^2) \right] \\ & + \frac{\omega^2 n_r}{2\pi^3 c^3} \Im \left[\mu_i g_{mm}^{11} + \varepsilon_i g_{ee}^{22} + \varepsilon_i \frac{\varepsilon^2}{|\varepsilon|^2} g_{ee}^{33} \right] \delta(z - z'). \end{aligned} \quad (\text{A6})$$

Substituting these to the general equations in¹³ allows simplifying the damping and scattering coefficients to their final forms given by

$$\alpha_{\pm,TE} = \frac{k_r k_0}{\rho_{TE}/\rho_0} \Im \left[\left(\frac{\zeta_{e,TE}}{\zeta_{v,TE}} + \zeta_{v,TE} \varepsilon_i \right) g_{ee}^{11} + \left(\frac{\zeta_{m,TE}}{\zeta_{v,TE}} + \zeta_{v,TE} \mu_i \right) g_{mm}^{22} \pm \zeta_{ex,TE} (g_{me}^{21} - g_{em}^{12}) + \zeta_{v,TE} \mu_i \frac{\mu^2}{|\mu|^2} g_{mm}^{33} \right], \quad (\text{A7})$$

$$\beta_{\pm,TE} = \frac{k_r k_0}{\rho_{TE}/\rho_0} \Im \left[\left(\frac{\zeta_{e,TE}}{\zeta_{v,TE}} - \zeta_{v,TE} \varepsilon_i \right) g_{ee}^{11} + \left(\frac{\zeta_{m,TE}}{\zeta_{v,TE}} - \zeta_{v,TE} \mu_i \right) g_{mm}^{22} \pm \zeta_{ex,TE}^* (g_{me}^{21} - g_{em}^{12}) - \zeta_{v,TE} \mu_i \frac{\mu^2}{|\mu|^2} g_{mm}^{33} \right], \quad (\text{A8})$$

$$\alpha_{\pm, TM} = \frac{k_r k_0}{\rho_{TM}/\rho_0} \Im \left[\left(\frac{\zeta_{m, TM}}{\zeta_{v, TM}} + \zeta_{v, TM} \mu_i \right) g_{mm}^{11} + \left(\frac{\zeta_{e, TM}}{\zeta_{v, TM}} + \zeta_{v, TM} \varepsilon_i \right) g_{ee}^{22} \pm \zeta_{ex, TM} (g_{em}^{21} - g_{me}^{12}) + \zeta_{v, TM} \varepsilon_i \frac{\varepsilon^2}{|\varepsilon|^2} g_{ee}^{33} \right], \quad (\text{A9})$$

$$\beta_{\pm, TM} = \frac{k_r k_0}{\rho_{TM}/\rho_0} \Im \left[\left(\frac{\zeta_{m, TM}}{\zeta_{v, TM}} - \zeta_{v, TM} \mu_i \right) g_{mm}^{11} + \left(\frac{\zeta_{e, TM}}{\zeta_{v, TM}} - \zeta_{v, TM} \varepsilon_i \right) g_{ee}^{22} \pm \zeta_{ex, TM}^* (g_{em}^{21} - g_{me}^{12}) - \zeta_{v, TM} \varepsilon_i \frac{\varepsilon^2}{|\varepsilon|^2} g_{ee}^{33} \right] \quad (\text{A10})$$

with the parameters and their equations given in the Supplemental Material of.¹³

Appendix B: Simulation parameters and other simulation details

Parameters used in the DD simulations of electron-hole transport are listed in Table I. The radiative recombination coefficient B is not used in the final IRTDD simulations, but an initial value of $7.2 \times 10^{-16} \text{ m}^3/\text{s}$ was used to get initial conditions. The A and C recombination coefficients are set to selected reasonable values for GaAs, and with these values the open-circuit voltage is still determined by radiative recombination. The A and C coefficients are the same for all the materials for simplicity, as recombination takes place predominantly in GaAs due to the relatively low injection levels.

For the optical simulations, we use photon energy-dependent complex dielectric functions reported in the literature for Au,²⁸ GaAs,²⁹ AlGaAs,³⁰ GaInP,³¹ AlInP,³² ZnS,³³ and MgF₂,³⁴ with help from.³⁵ The relative permeability is assumed to be 1 in all materials at all photon energies.

TABLE I: Parameters used in the DD simulations of electron-hole transport.^{26,27} The band offsets dE_c and dE_v are given with respect to the band edges in GaAs.

Property	GaAs	AlGaAs	InGaP	AlInP	Unit
ε	12.90	12.05	11.79	12.02	ε_0
E_g	1.43	1.84	1.91	1.62	eV
dE_v	0	-0.16	-0.31	-0.22	eV
dE_c	0	0.26	0.19	-0.03	eV
μ_n	8500	2300	2800	5400	$\text{cm}^2/(\text{Vs})$
μ_p	400	146	175	200	$\text{cm}^2/(\text{Vs})$
m_e^*	0.067	0.092	0.093	0.074	m_0
m_h^*	0.61	0.66	0.77	0.84	m_0
A	3×10^6				1/s
C	7×10^{-41}				m^6/s
B	N/A				m^3/s

¹ M. A. Green, Commercial progress and challenges for photovoltaics, Nat. Energy **1**, 15015 (2016).

² J. Cho, J. H. Park, J. K. Kim, and E. F. Schubert, White light-emitting diodes: History, progress, and future, Laser Photonics Rev. **11**, 1600147 (2017).

³ P. Bayvel, R. Maher, T. Xu, G. Liga, N. A. Shevchenko, D. Lavery, A. Alvarado, and R. I. Killey, Maximizing the optical network capacity, Phil. Trans. R. Soc. A. **374**, 20140440 (2016).

⁴ F. Cappelluti, D. Kim, M. van Eerden, A. P. Cédola, T. Aho, G. Bissels, F. Elsehrawy, J. Wu, H. Liu, P. Mulder, G. Bauhuis, J. Schermer, T. Niemi, and M. Guina, Light-trapping enhanced thin-film III-V quantum dot solar cells fabricated by epitaxial lift-off, Sol. Energ. Mat. Sol. C. **181**,

83 (2018).

⁵ H. Sai, T. Oku, Y. Sato, M. Tanabe, T. Matsui, and K. Matsubara, Potential of very thin and high-efficiency silicon heterojunction solar cells, Prog. Photovolt.: Res. Appl. **27**, 1061 (2019).

⁶ M. van Eerden, G. J. Bauhuis, P. Mulder, N. Gruginskie, M. Passoni, L. C. Andreani, E. Vlieg, and J. J. Schermer, A facile light-trapping approach for ultrathin GaAs solar cells using wet chemical etching, Prog. Photovolt.: Res. Appl., early view (2019).

⁷ I. Massiot, N. Vandamme, N. Bardou, C. Dupuis, A. Lemaître, J.-F. Guillemoles, and S. Collin, Metal Nanogrid for Broadband Multiresonant Light-Harvesting in Ultrathin GaAs Layers, ACS Photon. **1**, 878 (2014).

- ⁸ W. Metaferia, K. L. Schulte, J. Simon, S. Johnston, and A. J. Ptak, Gallium arsenide solar cells grown at rates exceeding $300 \mu\text{m h}^{-1}$ by hydride vapor phase epitaxy, *Nat. Commun.* **10**, 3361 (2019).
- ⁹ J. J. Schermer, P. Mulder, G. J. Bauhuis, P. K. Larsen, G. Oomen, and E. Bongers, Thin-film GaAs epitaxial lift-off solar cells for space applications, *Prog. Photovolt.: Res. Appl.* **13**, 587 (2005).
- ¹⁰ G. Timò, A. Martinelli, and L. C. Andreani, A new theoretical approach for the performance simulation of multijunction solar cells, *Prog. Photovolt.: Res. Appl.*, early view (2020).
- ¹¹ M. Wilkins, C. E. Valdivia, A. M. Gabr, D. Masson, S. Fafard, and K. Hinzer, Luminescent coupling in planar optoelectronic devices, *J. Appl. Phys.* **118**, 143102 (2015).
- ¹² A. W. Walker, O. Höhn, D. Neves Micha, B. Bläsi, A. W. Bett, and F. Dimroth, Impact of Photon Recycling on GaAs Solar Cell Designs, *IEEE J. Photovolt.* **5**, 1636 (2015).
- ¹³ M. Partanen, T. Häyrynen, and J. Oksanen, Interference-exact radiative transfer equation, *Sci. Rep.* **7**, 11534 (2017).
- ¹⁴ S. Chandrasekhar, *Radiative Transfer* (Dover, New York, 1960).
- ¹⁵ M. A. Steiner, J. F. Geisz, I. García, D. J. Friedman, A. Duda, and S. R. Kurtz, Optical enhancement of the open-circuit voltage in high quality GaAs solar cells, *J. Appl. Phys.* **113**, 123109 (2013).
- ¹⁶ P. Würfel, The chemical potential of radiation, *J. Phys. C* **15**, 3967 (1982).
- ¹⁷ M. Partanen, T. Häyrynen, J. Tulkki, and J. Oksanen, Quantized fluctuational electrodynamics for three-dimensional plasmonic structures, *Phys. Rev. A* **95**, 013848 (2017).
- ¹⁸ P. Kivisaari, M. Partanen, and J. Oksanen, Optical admittance method for light-matter interaction in lossy planar resonators, *Phys. Rev. E* **98**, 063304 (2018).
- ¹⁹ O. Heikkilä, J. Oksanen, and J. Tulkki, Ultimate limit and temperature dependency of light-emitting diode efficiency, *J. Appl. Phys.* **105**, 093119 (2009).
- ²⁰ ASTM G173-03(2012), Standard Tables for Reference Solar Spectral Irradiances: Direct Normal and Hemispherical on 37° Tilted Surface, ASTM International, West Conshohocken, PA, 2012, www.astm.org. Accessed August 15th, 2019.
- ²¹ H.-L. Chen, A. Cattoni, R. De Lépinau, A. W. Walker, O. Höhn, D. Lackner, G. Siefert, M. Faustini, N. Vandamme, J. Goffard, B. Behaghel, C. Dupuis, N. Bardou, F. Dimroth, and S. Collin, A 19.9%-efficient ultrathin solar cell based on a 205-nm-thick GaAs absorber and a silver nanostructured back mirror, *Nat. Energy* **4**, 761 (2019).
- ²² W. Yang, J. Becker, S. Liu, Y.-S. Kuo, J.-J. Li, B. Landini, K. Campman, and Y.-H. Zhang, Ultra-thin GaAs single-junction solar cells integrated with a reflective back scattering layer, *J. Appl. Phys.* **115**, 203105 (2014).
- ²³ B. Gai, Y. Sun, H. Lim, H. Chen, J. Faucher, M. J. Lee, and J. Yoon, Multilayer-Grown Ultrathin Nanostructured GaAs Solar Cells as a Cost-Competitive Materials Platform for III-V Photovoltaics, *ACS Nano* **11**, 992 (2017).
- ²⁴ H. Xu, A. Delamarre, B. M. F. Yu Jeco, H. Johnson, K. Watanabe, Y. Okada, J.-F. Guillemoles, Y. Nakano, and M. Sugiyama, Current transport efficiency analysis of multijunction solar cells by luminescence imaging, *Prog. Photovolt.: Res. Appl.* **27**, 835 (2019).
- ²⁵ M. P. Lumb, M. A. Steiner, J. F. Geisz, and R. J. Walters, Incorporating photon recycling into the analytical drift-diffusion model of high efficiency solar cells, *J. Appl. Phys.* **116**, 194504 (2014).
- ²⁶ I. Vurgaftman and J. R. Meyer, Band parameters for III-V compound semiconductors and their alloys, *J. Appl. Phys.* **89**, 5815 (2001).
- ²⁷ M. Levinshstein, S. Rumyantsev, and M. Shur, *Handbook Series on Semiconductor Parameters: Volume 1: Si, Ge, C (Diamond), GaAs, GaP, GaSb, InAs, InP, InSb* (World Scientific, Singapore, 1996).
- ²⁸ D. W. Lynch and W. R. Hunter, in *Handbook of Optical Constants of Solids*, edited by E. D. Palik (Academic Press, San Diego, 1998), pp. 286–295.
- ²⁹ E. D. Palik, in *Handbook of Optical Constants of Solids*, edited by E. D. Palik (Academic Press, San Diego, 1998), pp. 429–443.
- ³⁰ O. J. Glembocki and K. Takarabe, in *Handbook of Optical Constants of Solids*, edited by E. D. Palik (Academic Press, San Diego, 1998), pp. 513–558.
- ³¹ M. Schubert, V. Gottschalch, C. M. Herzinger, H. Yao, P. G. Snyder, and J. A. Woollam, Optical constants of $\text{Ga}_x\text{In}_{1-x}\text{P}$ lattice matched to GaAs, *J. Appl. Phys.* **77**, 3416 (1995).
- ³² M. Linnik and A. Christou, Calculations of optical properties for quaternary III-V semiconductor alloys in the transparent region and above (0.2–4.0 eV), *Phys. B: Cond. Matt.* **318**, 140 (2002).
- ³³ S. Ozaki and S. Adachi, Optical constants of cubic ZnS, *Jpn. J. Appl. Phys.* **32**, 5008 (1993).
- ³⁴ L. V. Rodríguez-de Marcos, J. I. Larruquert, J. A. Méndez, J. A. Aznárez, Self-consistent optical constants of MgF_2 , LaF_3 , and CeF_3 films, *Opt. Mater. Express* **7**, 989 (2017).
- ³⁵ M. N. Polyanskiy, "Refractive index database," <https://refractiveindex.info>. Accessed August 15th, 2019.